Strong structural and electronic coupling in metavalent PbS moiré superlattices

Yu Wang,[†,‡,⊥] Zhigang Song,[¶,⊥] Jiawei Wan,[†,§] Sophia Betzler,[†] Yujun Xie,[†] Colin Ophus,[‖] Karen C. Bustillo,[‖] Peter Ercius,[‖] Lin-Wang Wang,[†] and Haimei Zheng[*,†,§]

†*Materials Sciences Division, Lawrence Berkeley National Laboratory, Berkeley, CA 94720, USA.*

‡*Center for Electron Microscopy and South China Advanced Institute for Soft Matter Science and Technology, School of Emergent Soft Matter, South China University of Technology, Guangzhou 510640, China.*

¶*John A. Paulson School of Engineering and Applied Sciences, Harvard University, Cambridge, MA 02138, USA*

§*Department of Materials Science and Engineering, University of California, Berkeley, Berkeley, CA 94720, USA.*

‖*National Center for Electron Microscopy, The Molecular Foundry, Lawrence Berkeley National Laboratory, Berkeley, CA 94720, USA.*

⊥*Contributed equally to this work*

E-mail: hmzheng@lbl.gov

Abstract

Moiré superlattices are twisted bilayer materials, in which the tunable interlayer quantum confinement offers access to new physics and novel device functionalities. Previously, moiré superlattices were built exclusively using materials with weak van der

Waals interactions and synthesizing moiré superlattices with strong interlayer chemical bonding was considered to be impractical. Here using lead sulfide (PbS) as an example, we report a strategy for synthesizing moiré superlattices coupled by strong chemical bonding. We use water-soluble ligands as a removable template to obtain free-standing ultra-thin PbS nanosheets and assemble them into direct-contact bilayers with various twist angles. Atomic-resolution imaging shows the moiré periodic structural reconstruction at superlattice interface, due to the strong metavalent coupling. Electron energy loss spectroscopy and theoretical calculations collectively reveal the twist angle-dependent electronic structure, especially the emergent separation of flat bands at small twist angles. The localized states of flat bands are similar to well-arranged quantum dots, promising an application in devices. This study opens a new door to the exploration of deep energy modulations within moiré superlattices alternative to van der Waals twistronics.

Introduction

Recently, moiré superlattices have been synthesized by stacking two layers of two-dimensional (2D) materials with relative twist angles,[1,2] in which the long-range superlattice potentials from interlayer interactions can create quantum confinement in each layer. Quantum confinement in moiré superlattices can slow down or localize electrons, providing a tunable platform for studying strongly correlated physics,[3,4] such as superconductivity,[1,5] Mott insulators,[6] and interacting topological insulators.[7,8] In the moiré superlattices, the twisting topology determines the 2D quantum confinement and it offers an additional degree of freedom to modulate the electronic structure, usually referred to as twistronics.[9,10] So far, all 2D moiré superlattices are synthesized using van der Waals (vdW) materials,[11] such as graphene and transition-metal dichalcogenide, where the two layers of materials are coupled through vdW interactions. Twistronics based on these vdW materials has attracted great interest in various fields, ranging from physics[12–19] to materials science,[20–23] and chemistry.[24,25] Different

from materials coupled by chemical bonding at an interface, such as conventional semiconductor heterostructures, vdW twistronics have reduced strength in modulating the electronic structures due to the weak interlayer coupling, although strong coupling in twistronics is desired.[26,27] Most of the experimental observations of exotic electronic properties, especially those associated with electron transport, are realized at extremely low temperatures.[3,4,6–8,28] To increase the electronic modulation imposed by moiré superlattice, one approach is to replace the vdW interactions with strong chemical bonding such as covalent, ionic, or metavalent bonding.

Achieving strong quantum confinement in moiré superlattices by chemical bonding will pave a way to fabricating a new class of materials for beyond-vdW twistronics,[29] and it may also shed light on some challenging issues in other systems. For example, strongly coupled moiré superlattices can be structurally and functionally similar to an array of quantum dots,[30] offering an alternative route to super-crystals[31] by avoiding the notorious issue of connection defects formed during quantum dot self-assembly.[32] Moreover, the energy bands near the Fermi level in moiré patterns can be flattened due to the strong modulation, which may trap electrons in individual "quantum-dot" potentials upon suitable doping, leading to Wigner crystallization.[33–35] Thus, creating strongly coupled moiré superlattices through chemical bonding combines the strengths of two fields: the tunable confinement of 2D moiré superlattices and the strong coupling in conventional semiconductor heterostructures.

Despite of their promising unique features, chemically bonded moiré superlattices are unexplored due to the difficulty of synthesis. Having chemical bonding at moiré interfaces means that the materials are non-layered with intrinsically 3D crystalline structures, such as metals, II-VI semiconductors, and perovskites. Colloidal synthesis is a most important and common strategy to fabricate 2D nanocrystals with great material and structural versatility. It is natural to think assembling colloidal-synthesized 2D nanocrystals into chemically bonded superlattices. However, this requires a challenging ligand removal process, as ligands of 2D nanocrystals are principally designed to ligate strongly to guide asymmetric growth

and stabilize the formed nanocrystals.

Here, we use PbS as a model system to demonstrate a colloidal synthesis strategy for constructing chemically bonded moiré superlattices through the subtle design of removable ligands. Such beyond-vdW moiré superlattices are synthesized and examined for the first time. Strong interfacial coupling of the superlattice is revealed through atomic-resolution imaging, and the giant electronic modulation of moiré pattern is validated through the combination of electron energy loss spectroscopic analysis and theoretical calculations.

Results and discussion

Conceptual discussion of metavalent moiré superlattices

We first describe theoretically why chemically bonded moiré superlattices can give rise to stronger coupling effects than vdW moiré superlattices. As shown in Fig. 1a, bulk PbS has a rock-salt crystal structure and features an unconventional chemical bonding between Pb and S atoms, namely metavalent bonding. This term was created by theorists for specifically describing the fundamental bonding mechanisms of metal chalcogenides such as PbS, PbSe, and SnTe: the valence electrons in metavalent bonding are delocalized to an extent between covalent and ionic bonding.[25] This metavalent Pb–S bonding is much stronger than vdW interactions,[20] and it can be used as the interlayer interaction to construct strongly coupled PbS moiré superlattices if one can assemble ultra-thin 2D PbS nanosheets with pristine surfaces into twisted bilayers. This methodology may be further generalized to obtain new moiré superlattices coupled by other types of interfacial chemical bonding, for example, MXene[36] moiré superlattices coupled by metallic bonding, perovskite[37] moiré superlattices coupled by ionic bonding, and twisted bilayers of metal–organic frameworks[38] coupled by mixed interactions.

PbS moiré supercells with small commensurate angles have a tetragonal symmetry (Fig. 1b), in which two types of interfacial atoms stacked into four general configurations: Pb on

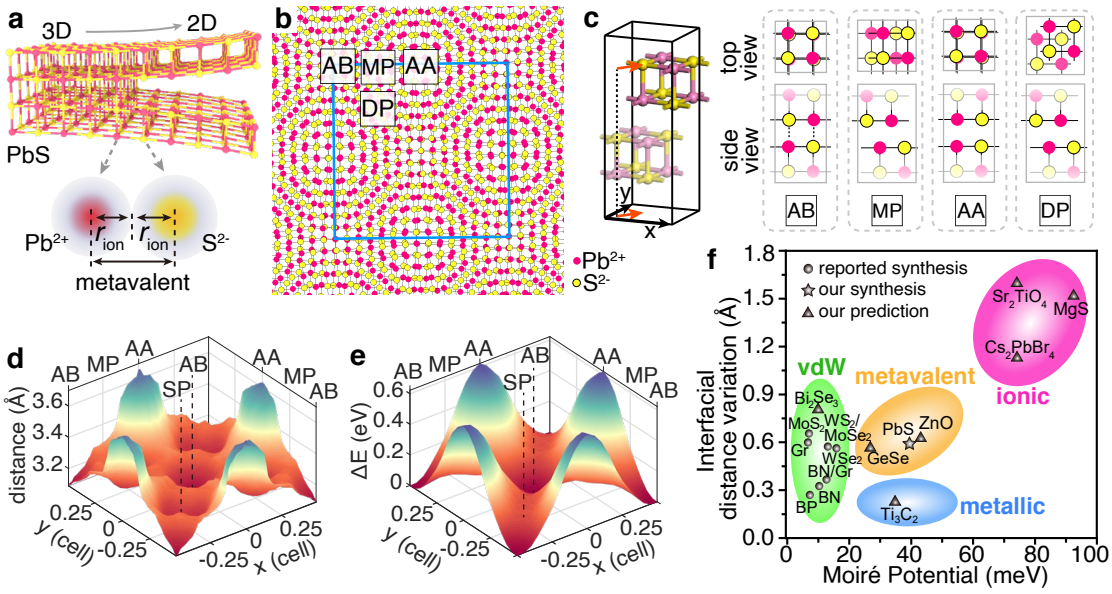

Figure 1: **Structure and strong coupling of PbS moiré superlattice**. **a**, 3D and the cleaved 2D structures of PbS rock-salt crystal, emphasizing the metavalent interaction in all directions. **b**, Different local atomic alignments occur in a PbS moiré superlattice with a twist angle of 8°. Blue square marks the moiré unit-cell. Four representative stacking configurations are highlighted as Pb on Pb (AA), Pb on S (AB), middle point (MP), and diagonal point (DP). **c**, Illustration of laterally shifting two PbS nanosheets for creating different stacking configurations. Top views and side views of representative structures are exemplified. **d**,**e**, DFT calculations of the structures created according to panel (c) showing the interfacial distance (d) and the free energy change (e) upon the bilayer lateral shift. **f**, DFT calculations on varieties of moiré superlattices, including the reported vdW superlattices, the metavalent PbS synthesized in this work, and our predictions of other chemically bonded superlattices. The results show their moiré potential and the largest interfacial distance variation among different stacking configurations.

Pb (marked as AA), Pb on S (marked as AB), the middle point (MP) between AA and AB, and the diagonal point (DP) between two AB positions. In small-angle twisted bilayers, each stacking configuration can be approximated by small unit cells consisting of laterally shifted bilayers, in which the shift coordinates are scaled by x and y in the unit of cell size (Fig. 1c). Therefore, the AB, AA, MP, and DP configurations correspond to the (x, y) of (0, 0), (0, 0.5), (0, 0.25), and (0.25, 0.25), respectively, and other configurations between the four extrema can be constructed with continuous (x, y) shift.

Density-functional theory (DFT) calculations on the created structures (detailed in Sup-

plementary Text S1) suggest that different stacking configurations can lead to deep modulations of interfacial reconstruction and electronic properties. Fig. 1d,e shows the changes of interlayer distance and free energy as functions of lateral interlayer shift. The surface plot regarding either interlayer distance or free energy has the maxima at AA spots and the minima at AB spots. The difference between the maximum and minimum interlayer distance is as large as 0.6 Å, implying a possible structural reconstruction at the interface of a small-angle twisted superlattice.

Maximal free energy fluctuation in the real space is defined as moiré potential,[16,39] which is an important indicator of the strength of energy modulation for a given moiré superlattice. We estimate the moiré potential of PbS and other 2D materials by calculating the largest free energy difference among all possible stacking configurations using approximate small unit cells. Fig. 1f shows the calculated moiré potentials of various materials, including the reported vdW superlattices, the metavalent PbS synthesized in this work, and our predictions of other chemically bonded superlattices. The moiré potential of PbS is 40 meV per atom, more than twice of the reported vdW superlattices. Generally, chemical bonding (e.g., metallic, metavalent, and ionic bonding) leads to much deeper energy modulation compared to vdW interactions. The deep energy modulation can localize electrons in the high-symmetry points with local energy extrema, providing an array of identical quantum-dot-like potentials.[30,31] Until now, the properties of the chemically bonded moiré superlattices and their structural stability remain unknown due to the lack of a synthesis strategy.

Synthesis of PbS moiré superlattices

Using metavalent PbS as a model system, we propose a colloidal synthesis strategy to construct chemically bonded moiré superlattices by employing moderately ligated and labile surfactant ligands. Strongly ligated ligands are typically necessary for guiding asymmetric growth during the colloidal synthesis of 2D nanocrystals. A commonly used ligand for synthesizing PbS nanocrystals is oleic acid, and removing it from inorganic core has been a

notorious problem in many related research, e.g., fully removal of oleic acid from quantum-dot surface is desired yet challenging.[40] Despite of previously reported synthesis of ultra-thin PbS nanosheets,[41] ligands are present in their laminated structures and prevent the direct contact of PbS cores.

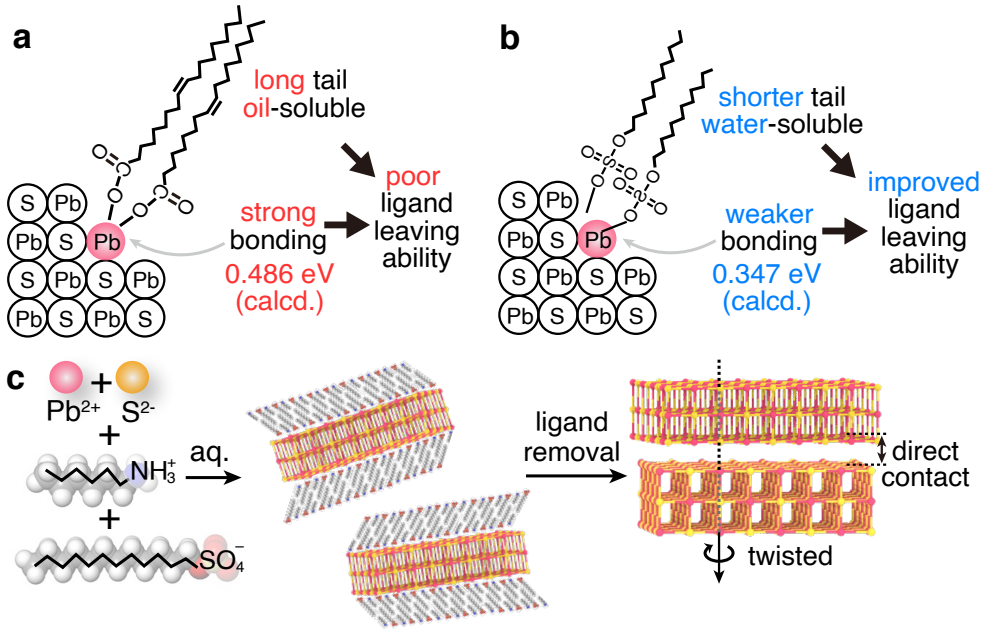

Figure 2: **Synthesis of PbS moiré superlattices enabled by readily removable ligands**. **a**, Features and calculated surface bonding energy of a commonly used oil-soluble ligand, oleic acid, for colloidal synthesis of PbS nanocrystals. **b**, As comparison, water-soluble dodecyl sulfate ligand has shorter chain and weaker surface bonding energy, improving the ligand leaving ability after aqueous colloidal synthesis. **c**, Schematics of aqueous colloidal synthesis of PbS moiré superlattices.

Analysing the ligand chemistry (Fig. 2a), we conjecture that the difficulty of removing oleic acid ligands comes from two aspects: 1. Ligand removal requires to occur in high-polar solvents (e.g., water) for breaking the Pb–carboxylic bonds and exposing the high-polar PbS surfaces. But oleic acid has a poor solubility in high-polar solvents due to its long-alkyl-chain. 2. The Pb–carboxylic bonding is relatively strong as it is commonly used for building metal–organic frameworks.[42] To overcome this problem, we develop an aqueous synthesis strategy employing two surfactant ligands that have adequate solubility and bind moderately with the inorganic core. As shown in Fig. 2b, dodecyl sulfate has a shorter

alkyl chain and a much better solubility in water over oleic acid. Our DFT calculations also indicate that dodecyl sulfate has a weaker bonding energy (0.347 eV) to PbS surface than that of oleic acid (0.486 eV), suggesting an improved ligand leaving ability.

Fig. 2c shows the synthesis schematic (details in Supplementary Method S1): Pb^{2+} and S^{2-} precursors and two water-soluble ligands (i.e., hexylamine and dodecyl sulfate) in an acidic aqueous solution at 80°C for 20 min produce ligand-capped ultra-thin PbS nanosheets. Then, the ligands are readily removed by washing with dilute basic and acidic aqueous solutions alternatively and rinsing with water. After ligand removal, the naked PbS nanosheets are immediately drop-cast, allowing the assembly of moiré superlattices through solvent evaporation .

Characterization of PbS moiré superlattices

TEM imaging and statistics (Fig.3a,b and Supplementary Fig. S1) show that the nanosheets have a rectangular shape with an average width and length of around 40 nm × 200 nm. Aberration-corrected transmission electron microscopy (TEM) imaging (Fig. 3c) and the zoomed-in portion from the yellow box (Fig. 3d) with corresponding image simulation (Fig. 3d inset) show that the as-synthesized nanosheets have a rock-salt structure with {001} surfaces and {110} edges. Energy-dispersive X-ray spectroscopy confirms that the moiré superlattice consists of Pb and S atoms at a molar ratio of 1:1 (Supplementary Fig. S2). We investigate the synthetic mechanism of PbS nanosheets by stopping the reaction earlier at 12 min and washing the product only twice with water. We observe the coexistence of PbS nanoparticles and nanosheets in the intermediate product as shown in Supplementary Fig. S3. The size distribution of nanoparticles is determined by image recognition and statistical analysis. Most nanoparticles have a diameter around 3 nm, approximate to the thickness of individual nanosheet (characterized from side view, shown in later section). Further characterization on intermediate products at various reaction time (Supplementary Fig. S4) shows that small particles with a diameter of 2–4 nm appear at 2 min and then grow

into platelets at 5 min. Fragmented sheets start to form after 8 min and grow into regular sheets in 20 min. Therefore, we conjecture that the aqueous synthesis of PbS nanosheets may undergo an oriented attachment process from nanoparticles to nanoplatelets, and then to nanosheets. A similar oriented attachment route has been proposed for the synthesis of PbS nanosheets in organic solvents.[41]

After self-assembly, bilayer moiré superlattices with various twist angles are observed at low magnification due to the presence of moiré fringes (Fig. 3e,f). A fast Fourier transform (FFT) of a representative moiré superlattice TEM image shows the expected pattern of two rotated sets of spatial frequencies corresponding to the structure of each sheet (Fig. 3f). In the enlarged images (bottom panels of Fig. 3f), the two red dots correspond to the (200) d-spacing of two individual sheets, the set of blue dots correspond to the d-spacings of the moiré pattern, and the orange dots correspond to the addition of the spatial frequencies from individual sheets and the moiré pattern. The theoretical relationship between the FFT pattern of an individual nanosheet and that of a moiré pattern is illustrated in Fig. 3g inset, and accordingly, the moiré d-spacing can be calculated by:

$$d_{\mathrm{m}}(200) = \frac{d_{\mathrm{rs}}(200)}{2 \cdot \sin(\theta/2)} \tag{1}$$

where θ is the twist angle; d_{m} and d_{rs} are the (200) d-spacing of the moiré cell and the rock-salt cell, respectively. In addition, the moiré d-spacing can also be directly measured from high-resolution TEM images for a variety of twist angles, verifying the calculated results from Eq. 1 as plotted in Fig. 3g.

Fig. 3h–j and Supplementary Fig. S5 show atomic-resolution TEM images and corresponding image simulations (blue images; see Supplementary Method S2) of moiré superlattices with various twist angles. For smaller twist angles, the (quasi-) unit cell of the moiré pattern is more obvious, and the superlattice appears as an array of identical quantum dots. For example, the moiré superlattice with a 3.2° twist angle (measured by the rotation angle

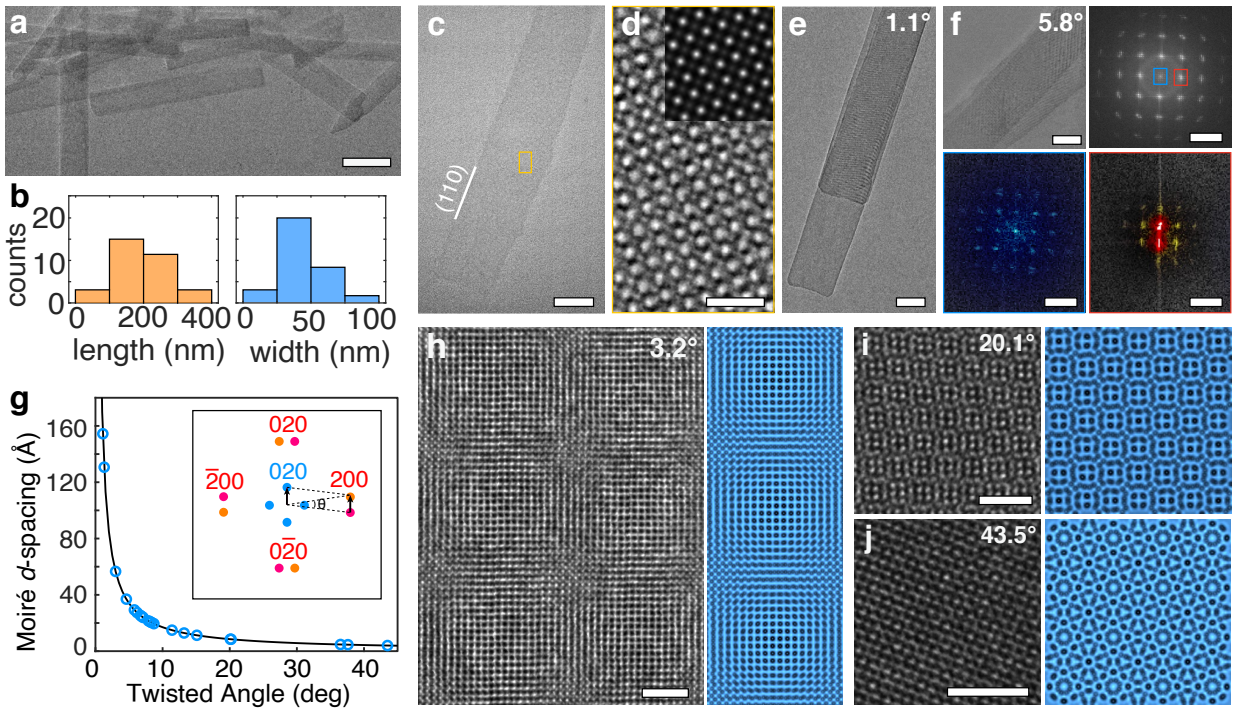

Figure 3: **TEM characterizations of PbS moiré superlattices**. **a**, A representative TEM image of synthesized ultra-thin PbS nanosheets. **b**, Size distribution of PbS nanosheets obtained from analysing (a) and Supplementary Fig. S1. **c**, Low magnification TEM image of a single PbS nanosheet. **d**, Atomic-resolution image of the boxed area in panel c with an inserted simulation of TEM image. **e**, TEM image of a bilayer moiré superlattice with a 1.1° twist angle. **f**, TEM image (top-left) and FFT pattern (top-right) of a bilayer moiré superlattice with a 5.8° twist angle. Two bottom panels show the enlarged details of the FFT pattern, in which blue dots indicate moiré spatial frequencies, red dots indicate the (200) spatial frequencies of two individual rock-salt nanosheets, and orange dots indicate the emerged pattern from moiré pattern and individual rock-salt patterns. **g**, Theoretical (black curve) and observed (green hollow dots) relationship between moiré d-spacing (200) and twist angles. Inset shows the relationship between moiré spatial frequencies (green) and two sets of individual rock-salt spatial frequencies (red and orange). **h**–**j**, Atomic-resolution TEM images and corresponding simulated images (false coloured) of bilayer moiré superlattices with a variety of twist angles. Scale bar:a, 50 nm; c, 30 nm; d, 1 nm; e, 100 nm; f, 30 nm (top left), 5 nm^{-1} (top right), 0.5 nm^{-1} (bottom two); h–j, 2 nm.

of FFT spots) consists of periodic AA/AB regions arranged in square symmetry with DP regions filled in the diagonal positions (Fig. 3h), resembling an epitaxially fused superlattice of 5∼6 nm PbS quantum dots.[32] At a large twist angle close to 45°, the moiré superlattice resembles 2D octagonal quasicrystals (Fig. 3j), showing an approximate C_8 symmetry in TEM image and reflecting the S_8 symmetry of octagonal quasicrystals.

Structural analysis of moiré superlattice interface

Fig. 4a shows the TEM image along the basal plane (side-view) of a moiré superlattice composed of three PbS sheets (labelled as S1, S2, and S3). The three sheets have a consistent thickness, approximately 3.0 nm, and consist of 10 (002) planes. Neighbouring sheets (S1–S2 or S2–S3) are in direct contact with 3 Å interfacial spacing and no trace of ligands at interface. For comparison, a bilayer with even one interfacial ligand residue would appear rather different, showing a larger interfacial distance over 5 Å (Supplementary Fig. S6). The clear interface between PbS sheets suggests the efficiency of the as-described ligand removal method.

Experimentally, one can evaluate whether an interface is coupled by chemical bonding or vdW interactions by measuring the inter-atom distance and analyzing if there is a vdW gap (as shown in Supplementary Fig. S7). For example, the covalent radius of carbon atom is 0.76 Å and the interlayer distance of graphene is 3.46 Å, hence the vdW gap is 1.94 Å. By contrast, the ionic radius of Pb^{2+} and S^{2-} are 1.33 Å and 1.84 Å,[43] respectively, giving an ionic bonding length of 3.17 Å. The measured interfacial distance in PbS twisted superlattices (Fig. 4c) is 3.35 Å, only slightly larger (0.18 Å) than the bonding length. Moreover, we have performed additional DFT calculations to elucidate the metavalent / chemical bonding of Pb–S. The calculated bonding energy is around 0.28 eV/bond, which is much larger than the typical vdW interaction (usually below 0.1 eV/bond).[44] For example, the vdW interaction in graphite is about 0.03 eV/bond.[45] Therefore, we evaluate that the PbS twisted superlattices are coupled by chemical bonding. To better visualize the bonding

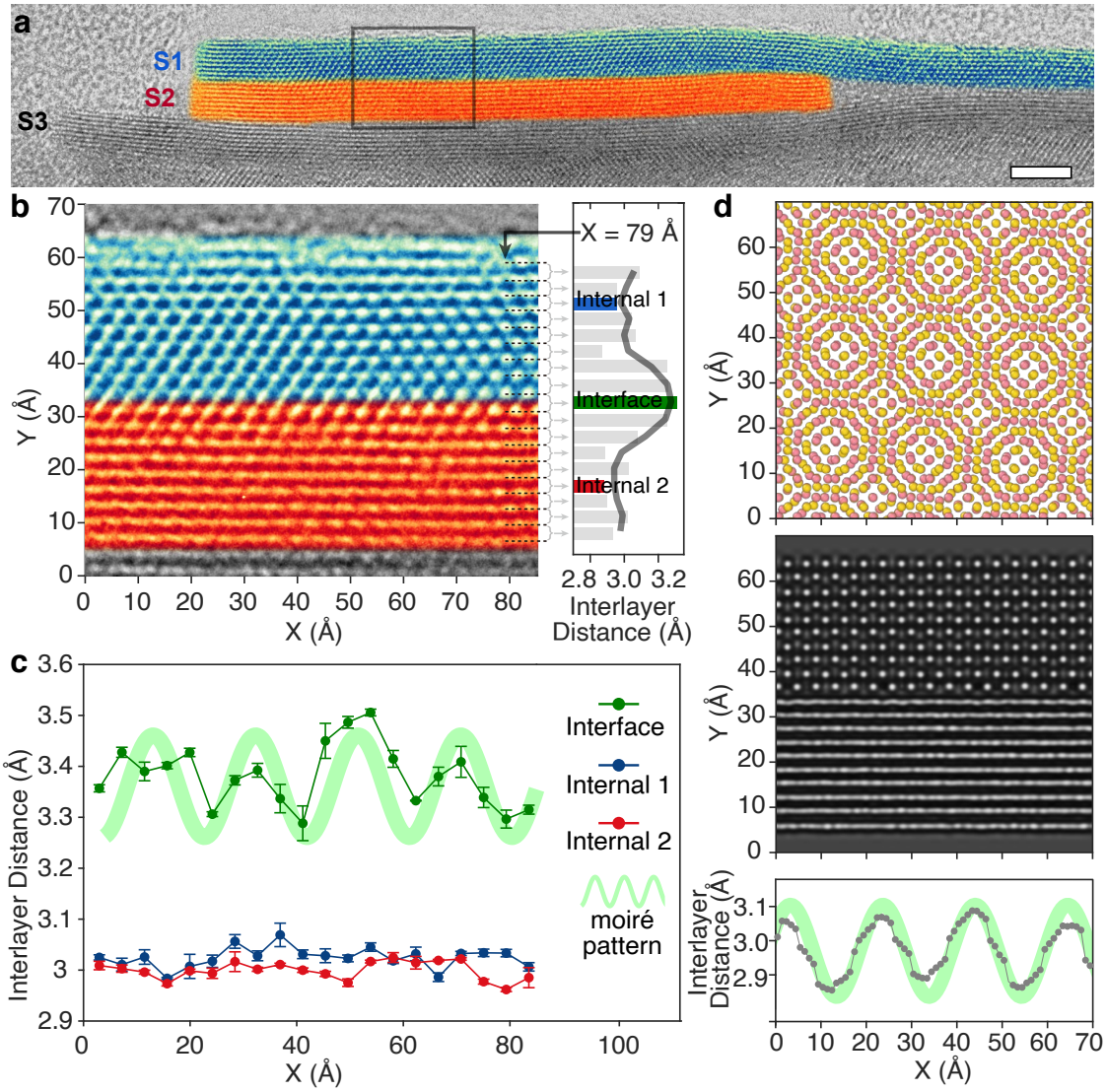

Figure 4: **Structural analysis of moiré superlattice interface**. **a**, Side view of a moiré superlattice composed of three sheets, S1, S2, and S3. S1 and S2 are false-coloured for clarity. Scale bar, 5 nm. **b**, Higher-resolution image of the boxed region in panel a and the demonstration of measuring interlayer distances. The Y positions of each layer (marked by dash lines) are evaluated by finding the brightest dots/strips in the image at the section of X = 79 Å, and the interlayer distances are calculated as the difference of neighbouring Y positions (marked by brackets and arrows). Two internal interlayers in each sheet and the interface of S1 and S2 are highlighted by blue, red, and green, respectively, as representative interlayers for further analysis in panel c. **c**, Interlayer distance fluctuation by measuring three representative interlayers at different X locations. Error bars indicate the standard deviation of measurements using three different sampling widths of 4, 6, and 8 Å. Thick green line shows the moiré periodicity of the bilayer superlattice with an 11.5° twist angle. **d**, Theoretically optimized atomic structure (up), simulated side-view image (middle), and calculated interfacial distance fluctuation (bottom, gray dots) of an 11.5° twist superlattice. Moiré periodicity (thick green line) for comparison.

at interface, we have also performed the electron population analysis of the 3.47° twisted superlattice. As shown in Supplementary Fig. S8, the Bloch states of bands are connected in different layer, demonstrating the interlayer bonding directly.

Furthermore, S1 and S3 are deformed beyond the right end of S2, indicating strong interlayer metavalent interactions and large deformability of naked PbS at the sub-10-nm scale.[46] This large deformability of uncoupled nanosheets is consistent with the self-rolling behaviour of individual naked nanosheets in the solution phase (Supplementary Text S2). Additionally, this also suggests that forming superlattices is an effective way to stabilize the naked nanosheets.

Further scrutiny of the side-view image in Fig. 4b reveals that S1 is oriented along a [110] axis regarding the viewing direction based on the observed elongated hexagonal pattern, whereas S2 is tilted away from a low-index zone axis. This indicates that the sheets are rotated around the basal plane regarding one another, confirming the formation of moiré superlattices with direct interlayer contact. We further measured the lattice spacings in the superlattice at different X locations in real space based on TEM image simulations and the recognition of the image peak positions, as detailed in Supplementary Text S3. The right graph in Fig. 4b shows an example at X = 79 Å, where the (002) spacings are approximate to 3.0 Å (similar to that in the bulk crystal) for the inner layers inside each sheet, but become slightly larger at the S1–S2 interface. We select two internal interlayers in each sheet (labelled as Internal 1 and 2) and the S1–S2 interface representative interlayers, and examine their interlayer spacing at different X locations. As shown in Fig. 4c, the spacings of Internal 1 and 2 are consistent to *c.a.* 3.0 Å with small fluctuation less than 0.1 Å, however, both the mean value (3.35 Å) and the fluctuation (over 0.2 Å) of interfacial spacing are considerably larger. Moreover, the fluctuation of interfacial spacing exhibits a periodicity that matches with the theoretical moiré periodicity of bilayer superlattice with a 11.5° twist angle. We simulate the side-view image of the theoretically optimized 11.5° twist superlattice and calculate the interfacial spacing in the simulated image (Fig. 4d). There is indeed a

considerable interfacial spacing fluctuation in the simulated image that matches with the theoretical moiré periodicity. The experimental and theoretical structural analysis jointly suggests the structural reconstruction at superlattice interface and its correlation to moiré periodicity.

Twist angle-dependent electronic states of moiré superlattices

We employ monochromated electron energy loss spectroscopy (EELS) in an aberration-corrected scanning TEM (STEM) to investigate the electronic excitation of moiré superstructures as a function of twist angle. Owing to the advantage of the latest direct detection camera and the large absorption efficiency of PbS, the low-loss spectra in the exciton region exhibit high signal-to-noise ratios (Supplementary Fig. S9). Fig. 5a shows the overview images of two representative superlattices with twist angles of 1.3° and 3.0° and the corresponding EELS scanning profiles. Other superlattices that were measured have larger twist angles 4.6°, 12°, and 35°. Because all moiré superlattices were measured in one experiment with identical conditions, we can compare the thickness of individual sheets from the scattering intensity from non-overlapping regions with only a single sheet in projection. We find that all individual nanosheets in the moiré superlattices have a similar thickness with less than 10% difference.

The integrated spectra of the double-layer regions with various twist angles are plotted in Fig. 5b, and the peak locations are extracted in Fig. 5c. These plots show that the spectral peak slightly shifts to lower energy as the twist angle decreases from 35.3° to 3.0°, but the peak energy dramatically decreases from 3.0° to 1.3°. This sudden decrease of peak energy at 1.3°is caused by the emergent peak split (red arrows in Fig.5b) at the positions of 1.62 eV and 1.77 eV, which is corresponding to the separation of emergent flat bands in small angle twist superlattices as demonstrated by the DFT calculations in later section.

Features in low-loss EEL spectra arise due to inter-band excitation and intra-band transitions in a similar way to optical spectra,[47,48] which are qualitatively reflective of the electronic

excitation or the bandgap. To understand the abrupt EELS peak change at small twist angle, we perform direct self-consistent calculations by constructing large moiré unit cells (up to 4360 atoms) with commensurate angles (Supplementary Text S1). The density of states (DOS) of the moiré cells with twist angles ranging from 4.47° to 43.6° are shown in Fig. 5d,

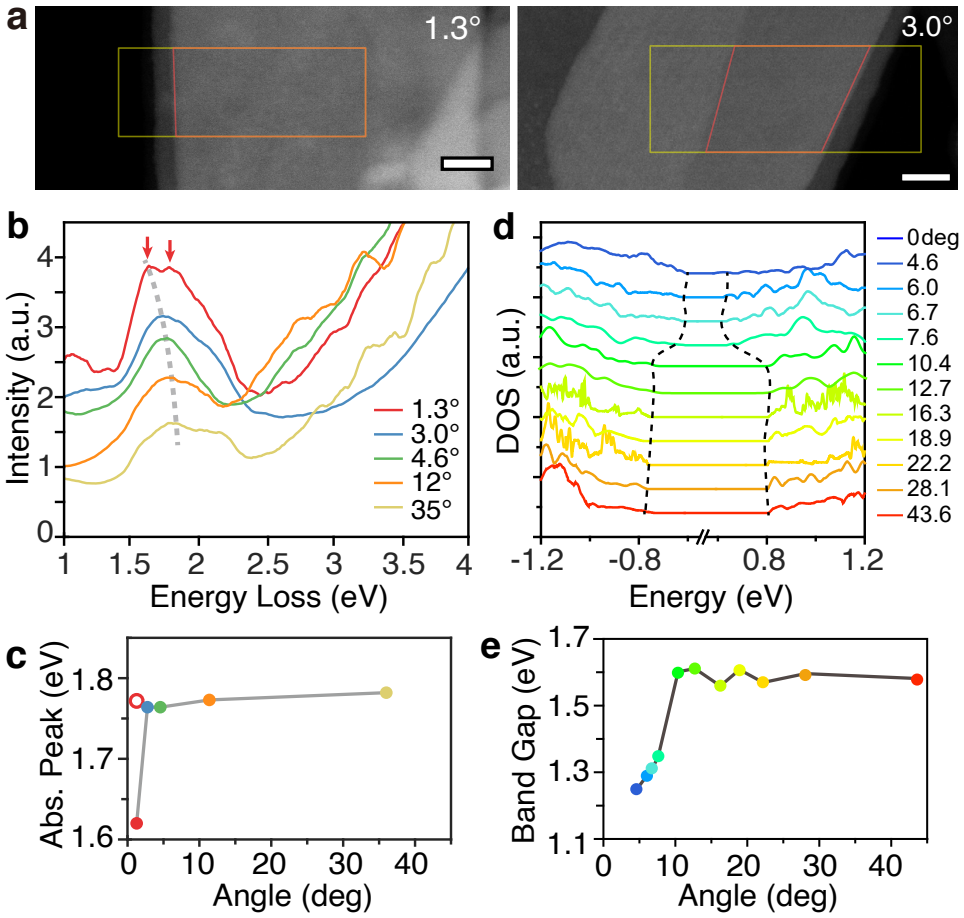

Figure 5: **Twist angle-dependent STEM-EELS and electronic states of moiré superlattices**. **a**, Overview images of two representative superlattices with twist angles of 1.3° and 3.0°. Yellow and red boxes mark the scanning regions and bilayer regions for STEM-EELS integration, respectively. Scale bar, 20 nm. **b**, Energy loss spectra of the bilayer regions of moiré superlattices with a variety of twist angles. Red arrows indicate the peak split at 1.3°. Energy dispersion of all spectra is 9 meV/pixel. **c**, Change of spectral peak upon twist angles extracted from panel b. Solid and hollow dots at 1.3°shows the position of two split peaks. **d**, Direct calculation of the density-of-states of commensurate moiré superlattices with a variety of twist angles. Black dashed lines connect the positions of first valence or conduction band for each structure. **e**, Bandgap change upon twist angles extracted from panel d.

and the corresponding bandgaps are plotted in Fig. 5e. For superlattices with a twist angle larger than 10.4°, the bandgap fluctuates around a constant. However, the bandgap drops rapidly as the twist angle decreases from 10.4° to smaller angles (Fig. 5e). The difference of critical angles in Figs. 5c and 5e is caused by two effects: 1. the necessary approximations used in DFT method, 2. our calculations are based on thinner moiré superlattices compared to the experimental structures due to the ultra-large computational cost (up to 4360 atoms). Because the atomic relaxation in thinner twisted structures is larger than that in thicker ones, the calculated critical angle is expected to be overestimated (i.e., larger than experimental one), details are shown in Supplementary Text S4. Despite of the quantitative offset, this calculated relationship between bandgap and twist angle, especially the sharp drop of bandgap at a small angle, is in good agreement with our EELS experiments (Fig. 5c). The experimental and theoretical results collectively suggest that the band structure of metavalent moiré superlattices, is highly dependent on the twist angle, especially at small twist angles.

Band structure calculations of PbS moiré superlattices

In addition to the twist angle-dependent bandgap, the DFT calculations of band structures reveal the emergent separation of electronic states of superlattices at small twist angles (Fig. 6a,b and Supplementary Fig. S10). As the twist angle of a superlattice falls below 10°, the bands become narrower due to the quantum confinement of the moiré pattern, and bands near the Fermi level begin to separate from the deep and high-energy states. For example, in the case of 3.47°, the bands near the Fermi level, especially the conduction band, become extremely flat (Fig. 6a,b). This emergent separation of electronic states is probably the reason of the observed peak split in the EELS spectrum at 1.3° (Fig. 5b). Supplementary calculations (Supplementary Fig. S10) show that the separation of moiré bands, which reflects the modulation effect by moiré pattern, becomes weaker as nanosheets become thicker. This separation of moiré bands, which reflects the modulation effect by moiré pattern, becomes

weaker as nanosheets become thicker. This thickness-dependent of modulation indicates the value of synthesizing ultra-thin free-standing nanosheets, stimulating future developments in the chemical and/or physical syntheses of ultra-thin beyond-vdW nanosheets and their strongly coupled moiré superlattices.

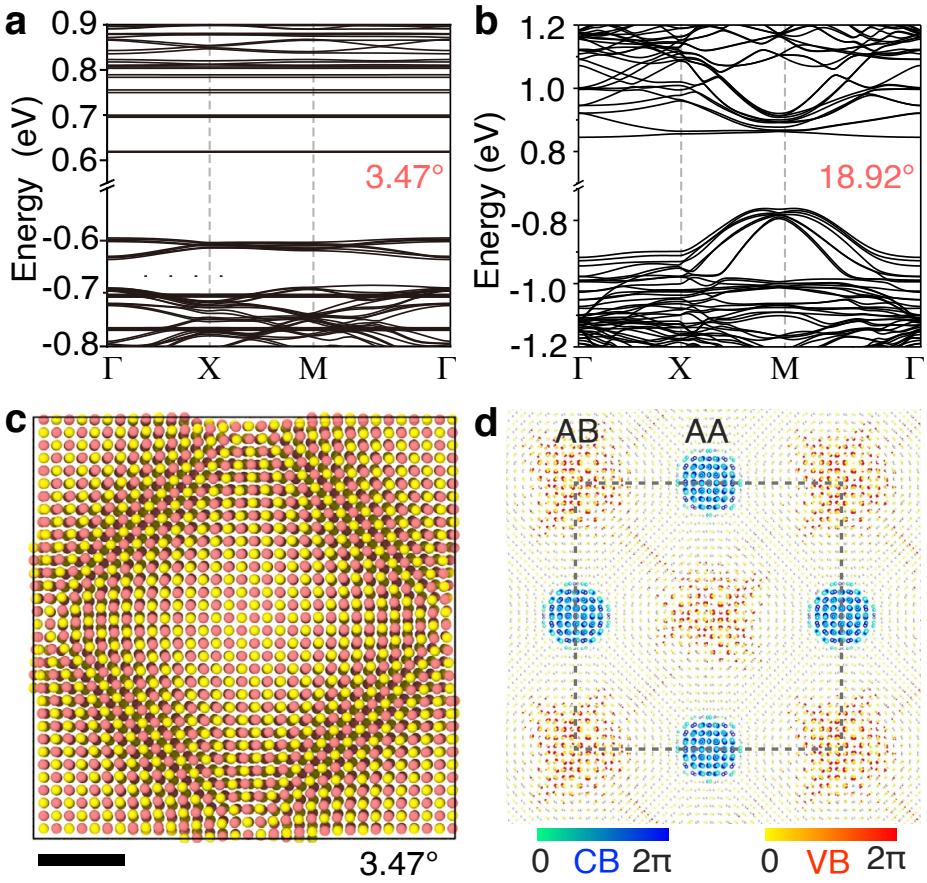

Figure 6: **DFT calculations of the electronic localization**. **a**,**b** Calculated band structures of the superlattices with twist angles of 3.47° and 18.92°. The thickness of calculated structures is four atomic layers. Fermi levels locate at 0 eV. **c**, Theoretically optimized moiré cell of the superlattice with a twist angle of 3.47°. Scale bar, 2 nm. **d**, Charge density of valence band (VB) and conduction band (CB) of the optimized structure in panel c. Colour is coded by the phase of wave function, ranging from 0 to 2π. Moiré cell is marked by the dashed line.

Furthermore, these separated moiré bands at small twist angles are highly spatially localized. Fig. 6d shows the corresponding wave functions of the conduction and valence bands, which are localized at AB and AA spots, respectively, with diameters of a few nanometres.

This also indicates that the PbS moiré superlattice not only structurally resembles but also functionally mimics a well-arranged array of quantum dots with separate energy levels and electron orbitals. Our additional calculation (Supplementary Text S5) suggests that the strong metavalent modulation by the moiré pattern may lead to emergent opto-electronic properties in valleytronics, such as valley-dependant optical selection rules.

Conclusion

We have established an approach to introduce strong metavalent interlayer interactions into moiré superlattices. Our synthesis strategy and findings on the chemically bonded moiré superlattices extend the current twistronics. Combining structural analysis, EELS measurements, and DFT calculations, we demonstrate that strong moiré modulation at a small twist angle can lead to considerable structural reconstruction and electronic renormalization. This study provides a route to arrays of identical "quantum-dot" potentials by achieving deep energy modulation through metavalent interactions, providing an alternative platform for spatially variant electronic and opto-electronic properties. For instance, the strong interlayer coupling may induce a series of giant strain vortices and dipole vortices and possibly nonlinear Hall effect. We anticipate that further experimental and theoretical studies on beyond-vdW moiré superlattices will find more types of interlayer interactions that may result in strong electronic coupling, strong correlation, and realizing tunable emergent quantum properties.

Acknowledgement

The work was supported by the U.S. Department of Energy (DOE), Office of Science, Office of Basic Energy Sciences (BES), Materials Sciences and Engineering Division under Contract No. DE-AC02-05-CH11231 within the KC22ZH program. Y.W. was partially supported by the UC Office of the President under the UC Laboratory Fees Research Program Collabo-

rative Research and Training Award LFR-17-477148. Work at the Molecular Foundry was supported by the Office of Science, Office of Basic Energy Sciences, of the U.S. Department of Energy under Contract No. DE-AC02-05CH11231.

Supporting Information Available

Supplementary figures including experimental procedures, characterization data, and band structures for PbS nanosheets and superlattices. Supplementary methods including TEM imaging, EELS measurements, and theoretical calculations. Supplementary text explaining the geometry, synthetic mechanism, simulation, and valleytronic properties of PbS superlattices.

References

(1) Cao, Y.; Fatemi, V.; Fang, S.; Watanabe, K.; Taniguchi, T.; Kaxiras, E.; Jarillo-Herrero, P. Unconventional superconductivity in magic-angle graphene superlattices. *Nature* **2018**, *556*, 43–50.

(2) Jin, C.; Regan, E. C.; Yan, A.; Utama, M. I. B.; Wang, D.; Zhao, S.; Qin, Y.; Yang, S.; Zheng, Z.; Shi, S.; Watanabe, K.; Taniguchi, T.; Tongay, S.; Zettl, A.; Wang, F. Observation of moiré excitons in WSe_2/WS_2 heterostructure superlattices. *Nature* **2019**, *567*, 76–80.

(3) Tang, Y.; Li, L.; Li, T.; Xu, Y.; Liu, S.; Barmak, K.; Watanabe, K.; Taniguchi, T.; MacDonald, A. H.; Shan, J., et al. Simulation of Hubbard model physics in WSe_2/WS_2 moiré superlattices. *Nature* **2020**, *579*, 353–358.

(4) Lu, X.; Stepanov, P.; Yang, W.; Xie, M.; Aamir, M. A.; Das, I.; Urgell, C.; Watanabe, K.; Taniguchi, T.; Zhang, G., et al. Superconductors, orbital magnets and correlated states in magic-angle bilayer graphene. *Nature* **2019**, *574*, 653–657.

(5) Arora, H. S.; Polski, R.; Zhang, Y.; Thomson, A.; Choi, Y.; Kim, H.; Lin, Z.; Wilson, I. Z.; Xu, X.; Chu, J.-H., et al. Superconductivity in metallic twisted bilayer graphene stabilized by WSe_2. *Nature* **2020**, *583*, 379–384.

(6) Cao, Y.; Fatemi, V.; Demir, A.; Fang, S.; Tomarken, S. L.; Luo, J. Y.; Sanchez-Yamagishi, J. D.; Watanabe, K.; Taniguchi, T.; Kaxiras, E.; Ashoori, R. C.; Jarillo-Herrero, P. Correlated insulator behaviour at half-filling in magic-angle graphene superlattices. *Nature* **2018**, *556*, 80–84.

(7) Nuckolls, K. P.; Oh, M.; Wong, D.; Lian, B.; Watanabe, K.; Taniguchi, T.; Bernevig, B. A.; Yazdani, A. Strongly correlated Chern insulators in magic-angle twisted bilayer graphene. *Nature* **2020**, *588*, 610–615.

(8) Chen, G.; Sharpe, A. L.; Fox, E. J.; Zhang, Y.-H.; Wang, S.; Jiang, L.; Lyu, B.; Li, H.; Watanabe, K.; Taniguchi, T., et al. Tunable correlated Chern insulator and ferromagnetism in a moiré superlattice. *Nature* **2020**, *579*, 56–61.

(9) Ribeiro-Palau, R.; Zhang, C.; Watanabe, K.; Taniguchi, T.; Hone, J.; Dean, C. R. Twistable electronics with dynamically rotatable heterostructures. *Science* **2018**, *361*, 690–693.

(10) Hu, G.; Ou, Q.; Si, G.; Wu, Y.; Wu, J.; Dai, Z.; Krasnok, A.; Mazor, Y.; Zhang, Q.; Bao, Q.; Qiu, C.-W.; Alú, A. Topological polaritons and photonic magic angles in twisted α-MoO_3 bilayers. *Nature* **2020**, *582*, 209–213.

(11) Carr, S.; Fang, S.; Kaxiras, E. Electronic-structure methods for twisted moiré layers. *Nat. Rev. Mater.* **2020**, *5*, 748–763.

(12) Dean, C. R.; Wang, L.; Maher, P.; Forsythe, C.; Ghahari, F.; Gao, Y.; Katoch, J.; Ishigami, M.; Moon, P.; Koshino, M., et al. Hofstadter's butterfly and the fractal quantum Hall effect in moiré superlattices. *Nature* **2013**, *497*, 598–602.

(13) Jiang, Y.; Lai, X.; Watanabe, K.; Taniguchi, T.; Haule, K.; Mao, J.; Andrei, E. Y. Charge order and broken rotational symmetry in magic-angle twisted bilayer graphene. *Nature* **2019**, *573*, 91–95.

(14) Uri, A.; Grover, S.; Cao, Y.; Crosse, J. A.; Bagani, K.; Rodan-Legrain, D.; Myasoedov, Y.; Watanabe, K.; Taniguchi, T.; Moon, P., et al. Mapping the twist-angle disorder and Landau levels in magic-angle graphene. *Nature* **2020**, *581*, 47–52.

(15) Sunku, S. S.; Ni, G. X.; Jiang, B. Y.; Yoo, H.; Sternbach, A.; McLeod, A. S.; Stauber, T.; Xiong, L.; Taniguchi, T.; Watanabe, K.; Kim, P.; Fogler, M. M.; Basov, D. N. Photonic crystals for nano-light in moiré graphene superlattices. *Science* **2018**, *362*, 1153–1156.

(16) Tran, K. et al. Evidence for moiré excitons in van der Waals heterostructures. *Nature* **2019**, *567*, 71–75.

(17) Alexeev, E. M. et al. Resonantly hybridized excitons in moiré superlattices in van der Waals heterostructures. *Nature* **2019**, *567*, 81–86.

(18) Seyler, K. L.; Rivera, P.; Yu, H.; Wilson, N. P.; Ray, E. L.; Mandrus, D. G.; Yan, J.; Yao, W.; Xu, X. Signatures of moiré-trapped valley excitons in $MoSe_2/WSe_2$ heterobilayers. *Nature* **2019**, *567*, 66–70.

(19) Sharpe, A. L.; Fox, E. J.; Barnard, A. W.; Finney, J.; Watanabe, K.; Taniguchi, T.; Kastner, M.; Goldhaber-Gordon, D. Emergent ferromagnetism near three-quarters filling in twisted bilayer graphene. *Science* **2019**, *365*, 605–608.

(20) Liu, Y.; Huang, Y.; Duan, X. Van der Waals integration before and beyond two-dimensional materials. *Nature* **2019**, *567*, 323–333.

(21) Sutter, P.; Wimer, S.; Sutter, E. Chiral twisted van der Waals nanowires. *Nature* **2019**, *570*, 354–357.

(22) Rhodes, D.; Chae, S. H.; Ribeiro-Palau, R.; Hone, J. Disorder in van der Waals heterostructures of 2D materials. *Nat. Mat.* **2019**, *18*, 541–549.

(23) Weston, A.; Zou, Y.; Enaldiev, V.; Summerfield, A.; Clark, N.; Zólyomi, V.; Graham, A.; Yelgel, C.; Magorrian, S.; Zhou, M., et al. Atomic reconstruction in twisted bilayers of transition metal dichalcogenides. *Nat. Nanotech.* **2020**, *15*, 592–597.

(24) Dong, R.; Zhang, T.; Feng, X. Interface-assisted synthesis of 2D materials: Trend and challenges. *Chem. Rev.* **2018**, *118*, 6189–6235.

(25) Kooi, B. J.; Wuttig, M. Chalcogenides by Design: Functionality through Metavalent Bonding and Confinement. *Adv. Mater.* **2020**, *32*, 1908302.

(26) Kazmierczak, N. P.; Van Winkle, M.; Ophus, C.; Bustillo, K. C.; Carr, S.; Brown, H. G.; Ciston, J.; Taniguchi, T.; Watanabe, K.; Bediako, D. K. Strain fields in twisted bilayer graphene. *Nat. Mater.* **2021**, *20*, 956–963.

(27) Shabani, S.; Halbertal, D.; Wu, W.; Chen, M.; Liu, S.; Hone, J.; Yao, W.; Basov, D. N.; Zhu, X.; Pasupathy, A. N. Deep moiré potentials in twisted transition metal dichalcogenide bilayers. *Nat. Phys.* **2021**, *17*, 720–725.

(28) Xu, Y.; Ray, A.; Shao, Y.-T.; Jiang, S.; Lee, K.; Weber, D.; Goldberger, J. E.; Watanabe, K.; Taniguchi, T.; Muller, D. A., et al. Coexisting ferromagnetic–antiferromagnetic state in twisted bilayer CrI_3. *Nat. Nanotech.* **2022**, *17*, 143–147.

(29) Kennes, D. M.; Claassen, M.; Xian, L.; Georges, A.; Millis, A. J.; Hone, J.; Dean, C. R.; Basov, D.; Pasupathy, A. N.; Rubio, A. Moiré heterostructures as a condensed-matter quantum simulator. *Nat. Phys.* **2021**, *17*, 155–163.

(30) Song, Z.; Sun, X.; Wang, L. Switchable Asymmetric Moiré Patterns with Strongly Localized States. *J. Phys. Chem. Lett.* **2020**, *11*, 9224–9229.

(31) Zhang, C.; Chuu, C.-P.; Ren, X.; Li, M.-Y.; Li, L.-J.; Jin, C.; Chou, M.-Y.; Shih, C.-K. Interlayer couplings, Moiré patterns, and 2D electronic superlattices in MoS_2/WSe_2 hetero-bilayers. *Sci. Adv.* **2017**, *3*, e1601459.

(32) Whitham, K.; Yang, J.; Savitzky, B. H.; Kourkoutis, L. F.; Wise, F.; Hanrath, T. Charge transport and localization in atomically coherent quantum dot solids. *Nat. Mat.* **2016**, *15*, 557–563.

(33) Wigner, E. Effects of the electron interaction on the energy levels of electrons in metals. *Trans. Faraday Soc.* **1938**, *34*, 678–685.

(34) Li, H.; Li, S.; Regan, E. C.; Wang, D.; Zhao, W.; Kahn, S.; Yumigeta, K.; Blei, M.; Taniguchi, T.; Watanabe, K., et al. Imaging two-dimensional generalized Wigner crystals. *Nature* **2021**, *597*, 650–654.

(35) Regan, E. C.; Wang, D.; Jin, C.; Bakti Utama, M. I.; Gao, B.; Wei, X.; Zhao, S.; Zhao, W.; Zhang, Z.; Yumigeta, K., et al. Mott and generalized Wigner crystal states in WSe_2/WS_2 moiré superlattices. *Nature* **2020**, *579*, 359–363.

(36) Naguib, M.; Mochalin, V. N.; Barsoum, M. W.; Gogotsi, Y. 25th anniversary article: MXenes: a new family of two-dimensional materials. *Adv. Mater.* **2014**, *26*, 992–1005.

(37) Ji, D.; Cai, S.; Paudel, T. R.; Sun, H.; Zhang, C.; Han, L.; Wei, Y.; Zang, Y.; Gu, M.; Zhang, Y., et al. Freestanding crystalline oxide perovskites down to the monolayer limit. *Nature* **2019**, *570*, 87–90.

(38) Wu, M.; Wang, Z.; Liu, J.; Li, W.; Fu, H.; Sun, L.; Liu, X.; Pan, M.; Weng, H.; Dincă, M., et al. Conetronics in 2D metal-organic frameworks: double/half Dirac cones and quantum anomalous Hall effect. *2D Mater.* **2016**, *4*, 015015.

(39) Halbertal, D.; Finney, N. R.; Sunku, S. S.; Kerelsky, A.; Rubio-Verdú, C.; Shabani, S.;

Xian, L.; Carr, S.; Chen, S.; Zhang, C., et al. Moiré metrology of energy landscapes in van der Waals heterostructures. *Nat. Commun.* **2021**, *12*, 242.

(40) Coropceanu, I.; Janke, E. M.; Portner, J.; Haubold, D.; Nguyen, T. D.; Das, A.; Tanner, C. P.; Utterback, J. K.; Teitelbaum, S. W.; Hudson, ¸ M. H., et al. Self-assembly of nanocrystals into strongly electronically coupled all-inorganic supercrystals. *Science* **2022**, *375*, 1422–1426.

(41) Schliehe, C.; Juarez, B. H.; Pelletier, M.; Jander, S.; Greshnykh, D.; Nagel, M.; Meyer, A.; Foerster, S.; Kornowski, A.; Klinke, C., et al. Ultrathin PbS sheets by two-dimensional oriented attachment. *Science* **2010**, *329*, 550–553.

(42) Zhang, C.; Wang, B.; Li, W.; Huang, S.; Kong, L.; Li, Z.; Li, L. Conversion of invisible metal-organic frameworks to luminescent perovskite nanocrystals for confidential information encryption and decryption. *Nat. Commun.* **2017**, *8*, 1138.

(43) Cordero, B.; Gómez, V.; Platero-Prats, A. E.; Revés, M.; Echeverría, J.; Cremades, E.; Barragán, F.; Alvarez, S. Covalent radii revisited. *Dalton Trans.* **2008**, 2832–2838.

(44) Lee, K.; Murray, É. D.; Kong, L.; Lundqvist, B. I.; Langreth, D. C. Higher-accuracy van der Waals density functional. *Phys. Rev. B* **2010**, *82*, 081101.

(45) Chakarova-Käck, S. D.; Schröder, E.; Lundqvist, B. I.; Langreth, D. C. Application of van der Waals density functional to an extended system: Adsorption of benzene and naphthalene on graphite. *Phys. Rev. Lett.* **2006**, *96*, 146107.

(46) Wang, Y.; Peng, X.; Abelson, A.; Xiao, P.; Qian, C.; Yu, L.; Ophus, C.; Ercius, P.; Wang, L.-W.; Law, M., et al. Dynamic deformability of individual PbSe nanocrystals during superlattice phase transitions. *Sci. Adv.* **2019**, *5*, eaaw5623.

(47) Hage, F. S.; Nicholls, R. J.; Yates, J. R.; McCulloch, D. G.; Lovejoy, T. C.; Dellby, N.;

Krivanek, O. L.; Refson, K.; Ramasse, Q. M. Nanoscale momentum-resolved vibrational spectroscopy. *Sci. Adv.* **2018**, *4*, eaar7495.

(48) Gogoi, P. K.; Lin, Y.-C.; Senga, R.; Komsa, H.-P.; Wong, S. L.; Chi, D.; Krasheninnikov, A. V.; Li, L.-J.; Breese, M. B.; Pennycook, S. J., et al. Layer rotation-angle-dependent excitonic absorption in van der Waals heterostructures revealed by electron energy loss spectroscopy. *ACS Nano* **2019**, *13*, 9541–9550.

TOC Graphic

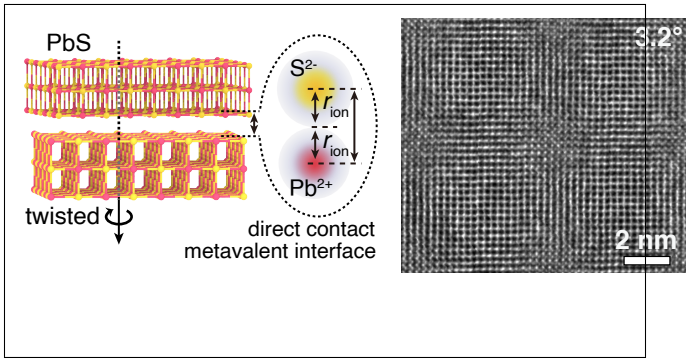
PbS
twisted
S2-
r ion
r ion
Pb2+
direct contact
metavalent interface
3.2°
2 nm